Solvent Molding of Organic Morphologies Made of Supramolecular Chiral Polymers

Luka Đorđević,[†,‡] Tomas Marangoni,[†,‡] Tanja Miletić,[†] Jenifer Rubio-Magnieto,[§] John Mohanraj,[⊥] Heinz Amenitsch,[∥] Dario Pasini,[#] Nikos Liaros,[×,∇] Stelios Couris,[×,∇] Nicola Armaroli,[⊥] Mathieu Surin,*,[§] and Davide Bonifazi*,[†,⊗]

[†]Department of Chemical and Pharmaceutical Sciences, INSTM UdR Trieste, University of Trieste, Piazzale Europa 1, 34127 Trieste, Italy

[§]Laboratory for Chemistry of Novel Materials, Center for Innovation in Materials and Polymers, University of Mons—UMONS, 20 Place du Parc, B-7000 Mons, Belgium

[⊥]Istituto per la Sintesi Organica e la Fotoreattività, Consiglio Nazionale delle Ricerche, Via Gobetti 101, 40129 Bologna, Italy

[∥]Institute of Inorganic Chemistry, Graz University of Technology, Stremayrgasse 9, 8010 Graz, Austria

[#]Department of Chemistry and INSTM UdR Pavia, University of Pavia, Viale Taramelli 10, 27100 Pavia, Italy

[×]Department of Physics, University of Patras, 26504 Patras, Greece

[∇]Institute of Chemical Engineering Sciences, Foundation for Research and Technology—Hellas, P.O. Box 1414, Patras 26504, Greece

[⊗]Namur Research College and Department of Chemistry, University of Namur—UNamur, Rue de Bruxelles 61, 5000 Namur, Belgium

S *Supporting Information*

ABSTRACT: The self-assembly and self-organization behavior of uracil-conjugated enantiopure (R)- or (S)-1,1′-binaphthyl-2,2′-diol (BINOL) and a hydrophobic oligo(p-phenylene ethynylene) (OPE) chromophore exposing 2,6-di(acetylamino)-pyridine termini are reported. Systematic spectroscopic (UV−vis, CD, fluorescence, NMR, and SAXS) and microscopic studies (TEM and AFM) showed that BINOL and OPE compounds undergo triple H-bonding recognition, generating different organic nanostructures in solution. Depending on the solvophobic properties of the liquid media (toluene, CHCl₃, CHCl₃/CHX, and CHX/THF), spherical, rod-like, fibrous, and helical morphologies were obtained, with the latter being the only nanostructures expressing chirality at the microscopic level.

SAXS analysis combined with molecular modeling simulations showed that the helical superstructures are composed of dimeric double-cable tape-like structures that, in turn, are supercoiled at the microscale. This behavior is interpreted as a consequence of an interplay among the degree of association of the H-bonded recognition, the vapor pressure of the solvent, and the solvophobic/solvophilic character of the supramolecular adducts in the different solutions under static and dynamic conditions, namely solvent evaporation conditions at room temperature.
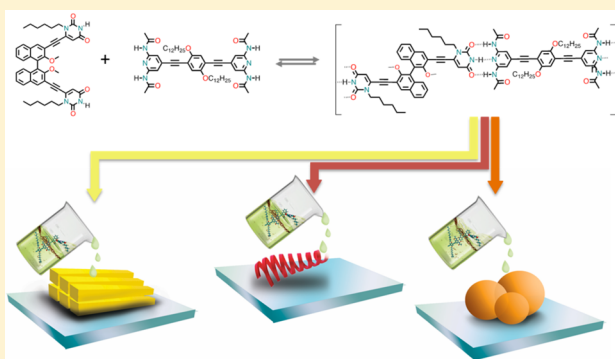
INTRODUCTION

Controlling and understanding the driving forces that govern the self-assembly and self-organization[1] of functional organic molecules into complex architectures are important research topics for developing nanostructured materials.[2] In this respect, chemists have developed several protocols to engineer functional architectures featuring programmed optoelectronic properties at different scales.[3] In particular, molecules possessing extended π-conjugated surfaces, such as oligo-(phenylene ethynylene)s (OPEs),[4] oligo(phenylenevinylene)s (OPVs),[3c,5] and coronene derivatives,[6] are versatile modules to prepare functional nanostructured materials due to their

tunable electronic and optical band gaps as well as their aptitude to arrange in π−π stacks. Further control of the organization can be achieved by using directional non-covalent interactions, such as multiple H-bonds[3a,c,e,7] and transition-metal coordination bonds.[8]

Whereas through molecular recognition the preparation of architectures with controlled function and shape can be easily reached at the molecular level by inserting the right functional groups in the self-assembling molecular constituents,[9] the

Scheme 1. (a) Molecules Prepared for This Study and (b) Synthetic Routes for Molecules (R)- or (S)-1, (R)- or (S)-3, 2, 4, and 5[a]
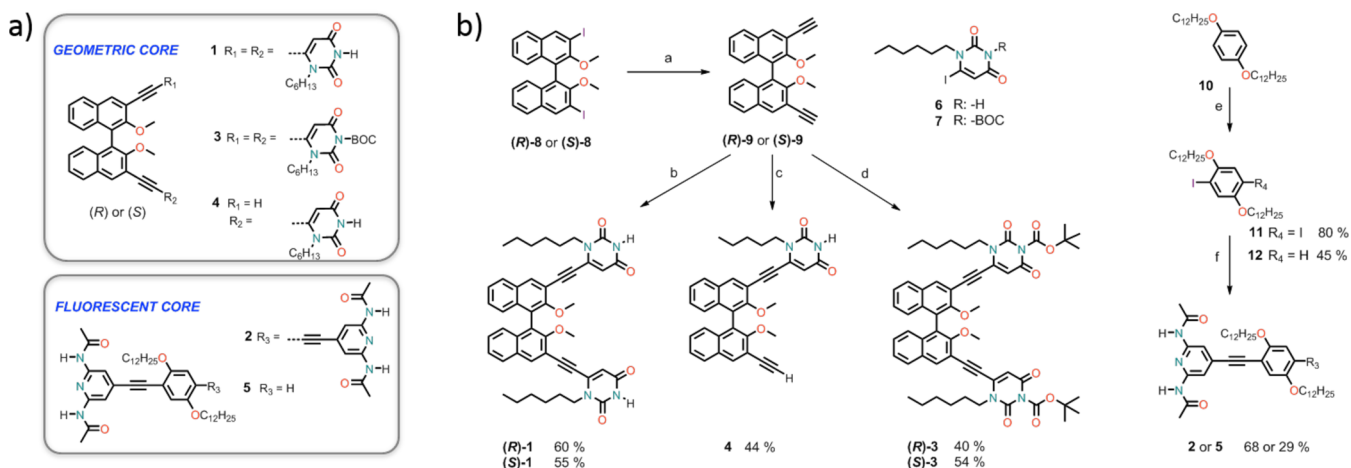
[a]Reagents and conditions: (a) (1) TMSA, Pd(PPh$_3$)$_2$Cl$_2$, CuI, Tol/Et$_3$N, rt; (2) K$_2$CO$_3$, THF, MeOH; (b) 6 (2.5 equiv), Pd(PPh$_3$)$_4$, CuI, THF/Et$_3$N, rt; (c) 6 (0.2 equiv), Pd(PPh$_3$)$_4$, CuI, THF/Et$_3$N, rt; (d) 7, Pd(PPh$_3$)$_4$, CuI, THF/Et$_3$N, rt; (e) Hg(OAc)$_2$, I$_2$ (2.5 or 1 equiv), CH$_2$Cl$_2$; (f) 2,6-di(acetylamino)-4-ethynylpyridine, Pd(PPh$_3$)$_4$, CuI, Tol/DMF/Et$_3$N. Abbreviations: TMSA, trimethylsilylacetylene; Tol, toluene; THF, tetrahydrofuran; DMF, dimethylformamide.

expression of the supramolecular structure properties at higher scales, and thus the full control of the morphological properties of microscopic structures, remains challenging.[7b,10]

In this respect, one significant problem to be tackled is the establishment of protocols capable of combining the effects of chemical structures and those of the boundary conditions, namely the solvent, interface, and temperature. From a mechanistic point of view, organic nanostructures generated by self-organization processes in solution are the result of a complex combination of several different variables. In particular, when organic materials are processed, the final morphologies are generally influenced by phenomena such as solvent dewetting and evaporation,[11] Ostwald ripening,[12] Rayleigh–Bénard instabilities,[13] Marangoni effect,[14] and phase separation.[15] Recently, we have shown that the geometric and spatial features of the organic morphologies generated by a supramolecular H-bonded polymer were ruled by local changes in the solution properties, leading to temperature-dependent non-equilibrium diffusion of the chemical species.[16] Only a limited number of efforts have been invested to elucidate the solvent effect on the self-organization of organic morphologies.[7d,10i,17] This is even more important if one wants to understand and control the transfer of molecular chirality at higher scales.[18]

We have been focusing for several years on the uracil·diamidopyridine (Ur·DAP) H-bonded complex as a hetero-molecular recognition motif for preparing different hierarchically organized materials.[19] With its moderate association constant, the Ur·DAP complex ensures a high degree of dynamicity and reversibility, requisite for establishing long-range molecular order[20] in liquids[19b,21] and at liquid–solid[22] and vacuum–solid interfaces.[23] With the aim of adding an additional piece towards the understanding of the expression of molecular chirality at higher dimensions, we prepared different molecular modules (Scheme 1) and studied their self-assembly and self-organization behavior in different solvents (chloroform (CHCl$_3$), toluene (Tol), chloroform/cyclohexane (CHCl$_3$/CHX) (1:1 v/v), and cyclohexane/tetrahydrofuran (CHX/THF)) by means of complementary spectroscopic (NMR, optical, and chiroptical characterization) and microscopic

techniques (Tapping Mode AFM and TEM). Instead of using chiral side chains, we have employed atropoisomeric chiral cores, which consist of a (R)- or (S)-1,1'-binaphthyl-2,2'-diol (BINOL).[24] This enantiomeric couple bears two Ur moieties, while the complementary DAP units are fixed at the extremities of a chromophoric OPE spacer with lateral solubilizing alkoxy chains. Atomic force microscopy (AFM) and transmission electron microscopy (TEM) showed a solvent-dependent formation of different organic morphologies. For instance, employing different CHX/THF solutions (80:20−95:5 v/v), nanostructures such as spheres, rods, or supercoiled helices were formed, with the last being the only morphologies expressing a certain degree of macroscopic chirality. Finally, small-angle X-ray scattering (SAXS) and molecular modeling simulations were used to shed additional light on the molecular organization of the helical morphologies, suggesting a tape-like hierarchical organization.

■ RESULTS AND DISCUSSION

Synthesis. Molecules (R)-1 and (S)-1 were synthesized by Pd-catalyzed Sonogashira−Hagihara cross-coupling reaction between enantiomerically pure 3,3'-diethynyl-2,2'dimethoxy-1,1'-binaphthalenes 9[25] and 1-hexyl-6-iodouracil 6.[23] BOC-protected compounds (R)-3 and (S)-3 were synthesized following an analogous pathway using N-BOC-protected 1-hexyl-6-iodouracil 7.[19b] While compound 2 was prepared according to our previously reported procedure,[21] compound 5 results from the Pd-catalyzed cross coupling of 2,6-di-(acetylamino)-4-ethynylpyridine with 1,4-bis(dodecyloxy)-2-iodobenzene 12.[21] Synthetic details are reported in Scheme 1b and Supporting Information (SI), Scheme S1. The compounds were characterized by ^{1}H and ^{13}C NMR spectroscopy, IR, HRMS, and optical activity (SI, Figures S1−S6).

NMR Investigations. The self-assembly of the complementary monotopic modules 4 and 5 was first studied to rationalize the influence of the lateral groups on the association behavior of the Ur·DAP recognition motif in solution (K_a, Table 1). Titration experiments in CDCl$_3$ (Figure 1a) showed a fast equilibrium, i.e., a progressive downfield shift of the uracil
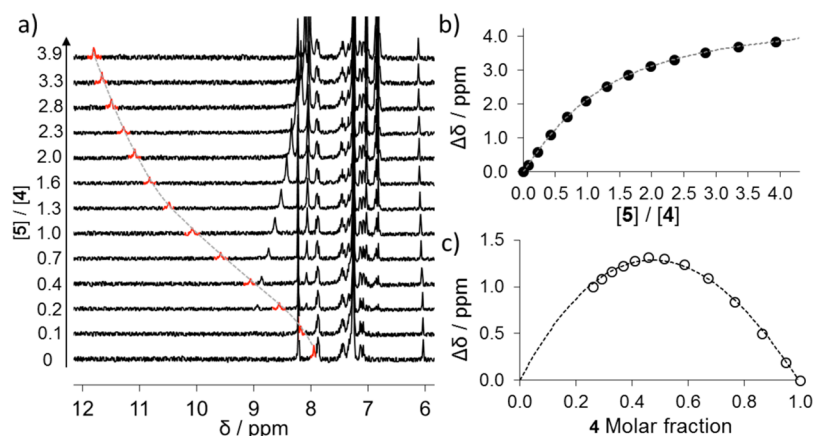
Figure 1. (a) ^1H NMR (400 MHz, 298 K) titration data of (S)-4 in $CDCl_3$ ($c = 1.3 \times 10^{-3}$ M) with different molar amounts of 5 (from 0 to 3.9 equiv). NH peaks are highlighted in red. (b) Titration data and 1:1 nonlinear least-squares fitting of the NH signals of (S)-4 plotted against the molar ratio. (c) Job's plot and fitting of the NH signals of (S)-4 plotted against the molar fraction.

Table 1. Calculated Association Constants (K_a) for the H-Bonded Heterodimer at 298 K for $4 + 5 \rightleftarrows [4 \cdot 5]$, Dimerization Constants (K_{dim}) for 4, and Corrected Association Constant (K_c) for $4 + 5 \rightleftarrows [4 \cdot 5]$, Considering the Dimerization of 4 in the Given Solvent[a]

solvent	ε_r	stoichiometry	K_a, M^{-1} (SD)	K_{dim}, M^{-1} (SD)	K_c, M^{-1} (SD)
$CDCl_3$	4.81	1:1	1296 (3)	7.5 (0.1)	1300 (29)
Tol-d_8	2.44	1:1	8737 (627)	60 (5)	8205 (564)
$CDCl_3$/CHX-d_{12}	/	1:1	14819 (3820)	19 (4)	14427 (3980)

[a]Calculations were performed with the Scientist package from MicroMath.

NH protons upon the incremental addition of 5. The association constant (Figure 1a,b) was found to be 1296($\pm$3) M^{-1} with a 1:1 stoichiometry (as evidenced by the continuous variation method, Figure 1c), values comparable to those reported in the literature for similar systems.[20b,22a] In more apolar solvents like Tol-d_8 and $CDCl_3$/CHX-d_{12} (1:1 v/v), K_a values of 8737($\pm$627) and 14819($\pm$3820) M^{-1} were measured, respectively (SI, Figure S7, and Table 1). As expected, increasing the apolar character of the solvent mixture favored an enhanced binding strength.[26] Dimerization constants of the Ur-bearing molecular modules were also measured in different solvents, i.e., 7, 19, and 60 M^{-1} in $CDCl_3$, $CDCl_3$/CHX-d_{12}, and Tol-d_8, respectively (see the dilution experiments as displayed in SI, Figure S8, and the fitting in SI, Figure S9, and Table 1), and were found to have only a negligible effect on the heteroassociation. This is in line with the literature reports.[27] Further NMR investigations confirmed the 1:2 and 2:1 binding stoichiometry for complexes $[1 \cdot (5)_2]$ and $[(4)_2 \cdot 2]$, respectively (SI, Figure S10). Considering the measured K_a values and assuming that the recognition motifs of the ditopic modules are independent, a mixture of complementary 1 and 2 molecules should lead to degrees of polymerization N^{28} of about 0.8, 2.1, and 2.7 in $CDCl_3$, Tol-d_8, and $CDCl_3$/CHX-d_{12} (1:1 v/v), respectively, when working under dilute conditions ($c = 2.5 \times 10^{-4}$ M).

NMR titrations in CHX/THF solutions could not be performed due to the limited solubility of both molecular components in the concentration interval needed for NMR. In order to corroborate the association of the supramolecular assemblies $[1 \cdot 2]_n$, ^1H NMR spectroscopy was performed on a 1:1 mixture of molecular modules (S)-1 and 2 (Figure 2a, spectra at $CDCl_3$, 500 MHz, 298 K) in $CDCl_3$. The addition of an equimolar quantity of 2 to a solution of (S)-1 induced a drastic downfield shift of the NH proton resonances, suggesting
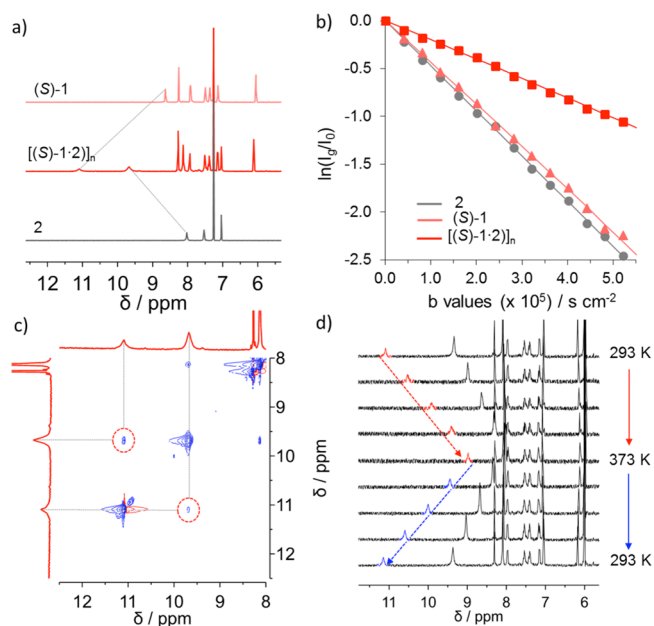

Figure 2. NMR characterization of supramolecular polymer $[(S)-1 \cdot 2]_n$. (a) ^1H NMR ($CDCl_3$, 500 MHz, 298 K) of (S)-1 (top), 2 (bottom), and supramolecular polymer $[(S)-1 \cdot 2]_n$ (middle). (b) DOSY-normalized signal decay versus the diffusion weighing (b values) for (S)-1 (pink), 2 (grey), and supramolecular polymer $[(S)-1 \cdot 2]_n$ (red). (c) 2D NOESY spectra ($CDCl_3$, 500 MHz, 298 K) of $[(S)-1 \cdot 2]_n$. (d) VT-NMR ($C_2D_2Cl_4$, 400 MHz) of $[(S)-1 \cdot 2]_n$ heating and cooling cycle.

the formation of the H-bonded complex (from 8.65 to 11.10 ppm and from 8.15 to 9.75 ppm for (S)-1 and 2, respectively), whereas all the other signals remained unaltered. $^1H-^1H$ NOESY (Figure 2c) analysis displayed the NH resonances

arising from the through-space interactions between the adjacent protons (NH-Ur and NH-DAP, respectively), suggesting, as expected, a close spatial proximity (<5 Å) between the Ur and DAP moieties. The non-covalent and reversible nature of the interaction was confirmed by variable-temperature (VT) NMR (400 MHz, $C_2D_2Cl_4$, Figure 2d and SI, Figure S12). Indeed, upon increasing the temperature from 293 to 373 K, a gradual re-instatement of the NH chemical shifts characteristic of molecules (**S**)-**1** and **2** alone was observed, clearly suggesting the disruption of the H-bonded complex, and thus that of the supramolecular assembly. Finally, diffusion ordered spectroscopy (DOSY) ($CDCl_3$, 500 MHz, 298 K, Figure 2b and SI, Figure S11) disclosed the presence of oligomeric species, in agreement with the predicted degree of polymerization N, featuring small diffusion coefficients $D_{[1·2]_n}$ = 2.00×10^{-6} cm^2 s^{-1} (compared to $D_1 = 4.37 \times 10^{-6}$ cm^2 s^{-1} and $D_2 = 4.70 \times 10^{-6}$ cm^2 s^{-1}) owing to the formation of high-molecular-weight oligomeric assemblies.[29]

Molding of the Morphologies. *Evaporation-Induced Polymerization.* As mentioned in the Introduction, the evaporation of a liquid solvent plays a crucial role in the formation of various nanostructures. This effect is known as evaporation-induced self-assembly (EISA).[30] As shown for inorganic architectures,[30] one can also expect that, in supramolecular polymerization, the vapor tension of a given liquid could play a dramatic role in the degree of polymerization. In a simple model, this depends on the association strength of the recognition motif, the monomer concentration, and the liquid vapor pressure at a given temperature. To evaluate these effects on our systems, we have investigated the polymerization behavior as a function of the evaporation rate of the solvent (Figure 3 and SI, Figure S13). Thus, we have
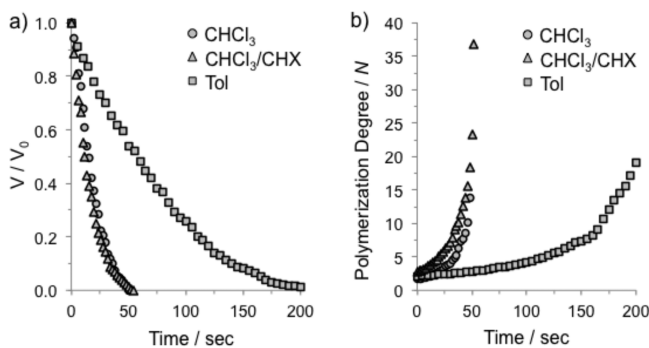

Figure 3. (a) Normalized evaporation of the solvents, reported as weight lost over time, and (b) estimated polymerization degree during evaporation. V and V_0 are the volume of the liquid at t and 0 s, respectively, calculated from the measured weight divided by the liquid density. Vapor tension (p_A) values at 20 °C and ambient pressure: 22 mmHg for Tol, 159 mmHg for $CHCl_3$, and 118 mmHg for the 1:1 v/v $CHCl_3$/CHX mixture (the latter value was calculated from Raoult's law).

measured the normalized time-dependent shrinking of a drop-casted liquid on an AFM support plate at room temperature in an open environment under ambient pressure. Depending on the vapor pressure of the liquid, a progressive increase in the concentration of the monomers is observed, thus dynamically affecting the degree of polymerization.[31] As outlined in Figure 3, the higher the liquid vapor pressure (p_A), the larger the maximum degree of polymerization; for instance, at the 50 s time point, the estimated N is ~15 for a solvent with higher p_A

($CHCl_3$) and ~3 for a solvent with a lower p_A (Tol). This suggests that, in evaporating $CHCl_3$ solutions, the organic morphologies are mainly controlled by the formation of longer polymers, while in Tol very short oligomers are preferentially formed. On the other hand, solutions with similar evaporation rates give degrees of polymerization essentially controlled by the association strength of the recognition unit. For instance, in the 1:1 v/v $CHCl_3$/CHX mixture, a higher degree of polymerization can be achieved (~40) than in $CHCl_3$ after 50 s, owing to the stronger association of the Ur·DAP motif in apolar solutions.

In this model, however, we did not consider the solvophobic and solvophilic properties of the solvent with respect to the monomers and the supramolecular assemblies. As previously observed for similar systems, the evaporation of the solvent can also lead to concentration-driven solutal instabilities,[16] inducing precipitation phenomena, aggregation, or polymerization termination. This effect will be qualitatively considered for each solvent in the discussions of the next paragraphs.

$CHCl_3$: From Solution to Nanorods. Due to the chromophoric nature of the OPE spacer, UV–vis spectra of dilute solutions were measured to gain insight into the self-assembly process. Under dilute conditions ($c = 2.5 \times 10^{-4}$ M) in $CHCl_3$, no discernible changes in the absorption profiles of $[1·2]_n$ compared to the individual compounds were noticed (SI, Figure S14), due to the weak degree of association of the Ur·DAP complex. However, when a solution of $[1·2]_n$ (1.3×10^{-3} M) was drop-casted onto freshly cleaved mica or carbon-coated grids, aggregation was observed, and different nanoscopic morphologies were visualized by TM-AFM and TEM. Both techniques confirmed the presence of rod-like microstructures featuring diameters between 150 and 500 nm and lengths ranging from 0.5 to 6.5 μm. Through the combined use of both TEM and AFM imaging (Figure 4 and SI, Figure S27), it was possible to discern rod-like structures composed of bundles of smaller fibers exhibiting a diameter of approximately 6 nm. Based on the above consideration, we can interpret these fibers as formed by short supramolecular polymers ($N \simeq 15-20$) that upon formation undergo aggregation, affording the macroscopic constitutional unit of the observed morphologies. Relying on the onset condition of a concentration-driven solutal instability,[16] the extensive aggregation phenomenon seems to be governed by the solvophobic lateral alkoxy chains of compound **2**. It can be hypothesized that the $OC_{12}H_{25}$ chains are somewhat exposed on the external side of the polymeric assemblies, forming a hydrophobic coat that enables extensive van der Waals interactions through chain–chain interdigitation, ultimately driving the formation of the aggregated morphologies.

Toluene: From Solution to Amorphous Nanoparticles. Subsequently, the influence of toluene on the self-assembly was studied. The UV–vis profile of $[1·2]_n$ ($c = 2.5 \times 10^{-4}$ M) showed a red shift ($\lambda = 388$ nm to $\lambda = 397$ nm) of the $\pi-\pi^*$ transition of the OPE derivative **2** and the formation of a shoulder at around 415 nm (Figure 5a). Variable-temperature measurements showed the appearance of an isosbestic point ($\lambda = 403$ nm) and an absorption profile that shifted toward the algebraic sum of the individual components (Figure 5b and SI, Figures S18 and S19). Notably, the spectra were more intense at higher temperatures, suggesting a low solubility of compound **2** in toluene solutions at room temperature (low solubility of compound **2** was confirmed by VT-UV–vis measurements, see SI, Figure S20).[32]
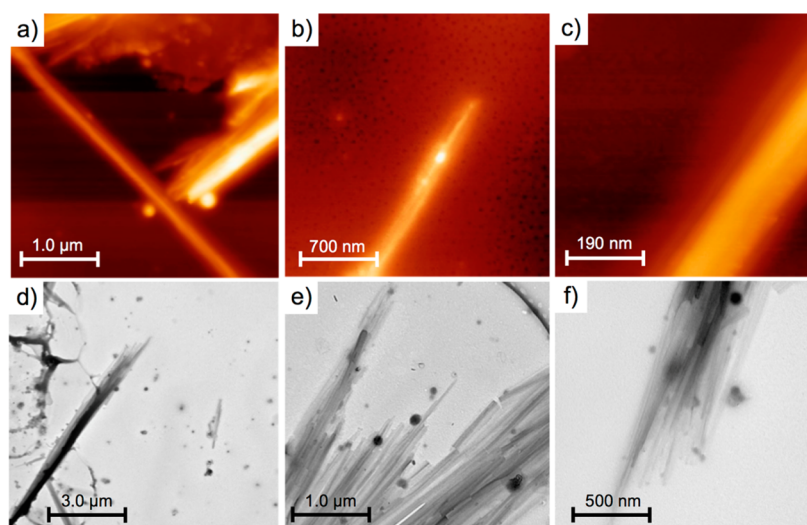
Figure 4. TM-AFM (a−c) and TEM (d−f) images of the morphologies obtained from a drop-casted $CHCl_3$ solution of $[(S)\text{-}\mathbf{1}\cdot\mathbf{2}]_n$ ($c = 1.3 \times 10^{-3}$ M); the other enantiomer showed the same type of nanostructuring (Supporting Information, Figure S27).

Owing to the intrinsic chirality of (R)-$\mathbf{1}$ or (S)-$\mathbf{1}$ and the favorable association of the Ur·DAP complex in toluene, it was possible to study the chiral assemblies by circular dichroism (CD) spectroscopy on both the pure components and the relative assemblies. The CD spectra ($c = 2.5 \times 10^{-4}$ M) of the BINOL derivatives were characterized by a maximum at 352 nm and an overall CD effect, which takes place in the region between 290 and 380 nm (Figure 5c). When linear module $\mathbf{2}$
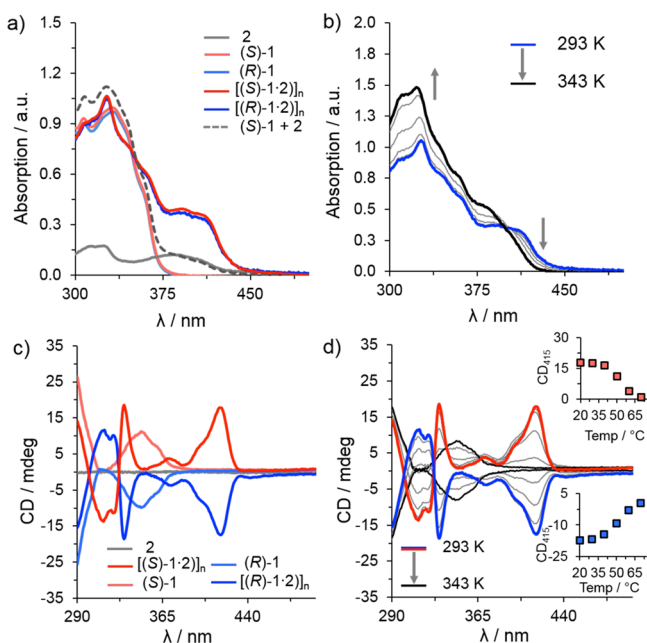

Figure 5. (a) Electronic absorption spectra of (S)-$\mathbf{1}$, (R)-$\mathbf{1}$, $\mathbf{2}$, $[(S)\text{-}\mathbf{1}\cdot\mathbf{2}]_n$, and $[(R)\text{-}\mathbf{1}\cdot\mathbf{2}]_n$ in toluene at 293 K ($c = 2.5 \times 10^{-4}$ M). (b) Variable-temperature absorption spectral changes in toluene from 293 to 343 K ($c = 2.5 \times 10^{-4}$ M, recorded each 5 K at a rate of 1 K/min); the same behavior was observed for the other enantiomer. (c) CD spectra of (S)-$\mathbf{1}$, (R)-$\mathbf{1}$, $\mathbf{2}$, $[(S)\text{-}\mathbf{1}\cdot\mathbf{2}]_n$, and $[(R)\text{-}\mathbf{1}\cdot\mathbf{2}]_n$ in toluene at 293 K ($c = 2.5 \times 10^{-4}$ M). (d) VT-CD spectral changes of $[(S)\text{-}\mathbf{1}\cdot\mathbf{2}]_n$ and $[(R)\text{-}\mathbf{1}\cdot\mathbf{2}]_n$ in toluene from 293 to 343 K ($c = 2.5 \times 10^{-4}$ M, recorded each 10 K at a rate of 1 K/min; the inset shows the CD intensity (at $\lambda = 415$ nm) plotted versus temperature.

was added to a solution of (R)-$\mathbf{1}$ or (S)-$\mathbf{1}$, a new signal appeared in the region 390−435 nm with a peak around 415 nm and a shoulder around 400 nm (Figure 5c), a spectral region in which the BINOL derivatives are not CD active. To further investigate this induced CD effect in the region where achiral $\mathbf{2}$ absorbs, the CD spectra were recorded as a function of temperature and concentration for both $[(S)\text{-}\mathbf{1}\cdot\mathbf{2}]_n$ and $[(R)\text{-}\mathbf{1}\cdot\mathbf{2}]_n$ assemblies (Figure 5d and SI, Figure S24). VT-CD experiments from 293 to 343 K for $[\mathbf{1}\cdot\mathbf{2}]_n$ showed a gradual decrease of the induced CD effect at 415 nm, which is in accordance with the VT-UV−vis measurements. Surprisingly, drop-casting from a toluene solution of $[\mathbf{1}\cdot\mathbf{2}]_n$ ($c = 2.5 \times 10^{-4}$ M) onto mica showed only the presence of globular, yet undefined, aggregates (SI, Figure S28). This suggests that, as the solvent evaporates, the forming supramolecular assemblies undergo solutal instability already at short lengths, thus giving rise to non-structured morphologies most likely controlled by a fast matter-momentum transport in solution.

CHCl₃/CHX: From Solution to Nanofibers. The absorption profile of $[\mathbf{1}\cdot\mathbf{2}]_n$ in $CHCl_3$/CHX (1:1 v/v, $c = 2.5 \times 10^{-4}$ M) displayed a red shift ($\lambda = 383$ nm to $\lambda = 390$ nm) of the $\pi–\pi^*$ transition of compound $\mathbf{2}$ and the formation of a shoulder at $\lambda = 410$ nm (Figure 6a). On increasing the temperature from 293 to 333 K, the absorption spectra underwent a gradual hypsochromic shift. The spectral shape at 333 K resembled those of the single components at room temperature, thus suggesting the disruption of the aggregates (SI, Figure S15). As expected, the absorption profiles were identical when the experiments were performed with (R)-$\mathbf{1}$ or (S)-$\mathbf{1}$. Additional experiments (VT-UV−vis and CD) with reference molecules $\mathbf{4}$ and $\mathbf{5}$, BOC-protected molecules $\mathbf{3}$, and molecules $\mathbf{1}$ and $\mathbf{2}$ alone did not show any significant changes in the absorption profile (SI, Figures S16, S17, and S21), indicating that the spectral changes in $[\mathbf{1}\cdot\mathbf{2}]_n$ are attributed to the changes of the supramolecular assembly. The same behavior was also observed by CD spectroscopy (SI, Figures S22 and S23).

In $CHCl_3$/CHX (1:1 v/v), the CD spectra ($c = 2.5 \times 10^{-4}$ M) of the BINOL derivatives were characterized by CD signals between 250 and 390 nm (Figure 6b). When linear module $\mathbf{2}$ was added to a solution of (R)-$\mathbf{1}$ or (S)-$\mathbf{1}$, a new signal appeared in the region 390−440 nm with a maximum at around
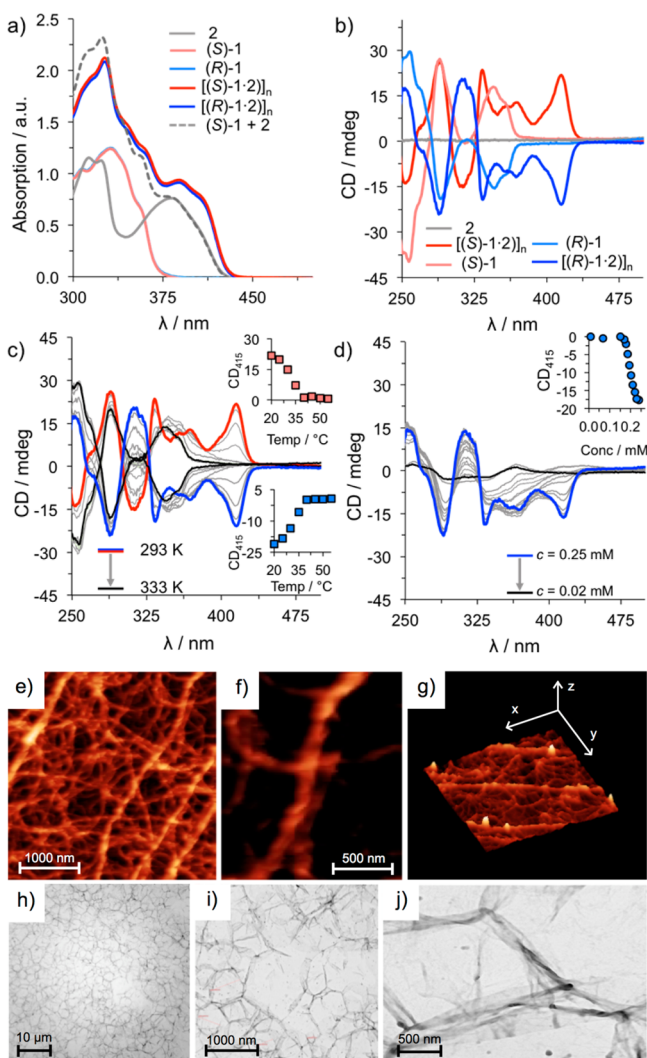
Figure 6. (a) Electronic absorption spectra of (S)-1, (R)-1, 2, [(S)-1·2]$_n$, and [(R)-1·2]$_n$ in CHCl$_3$/CHX (1:1 v/v) at 293 K (c = 2.5 × 10^{-4} M). (b) CD spectra of (S)-1, (R)-1, 2, [(S)-1·2]$_n$, and [(R)-1·2]$_n$ in CHCl$_3$/CHX (1:1 v/v) at 293 K (c = 2.5 × 10^{-4} M). (c) VT-CD spectral changes of [(S)-1·2]$_n$ and [(R)-1·2]$_n$ in CHCl$_3$/CHX (1:1 v/v) from 293 to 333 K (c = 2.5 × 10^{-4} M, recorded each 5 K at a rate of 1 K/min); insets show plot of CD intensity (λ = 415 nm) versus temperature. (d) Variable-concentration CD spectral changes of [(R)-1·2]$_n$ in CHCl$_3$/CHX (1:1 v/v) at 293 K; inset shows plot of CD intensity (λ = 415 nm) versus concentration. The same behavior was also observed with the other enantiomer. (e–g) TM-AFM and (h–j) TEM images of the morphologies obtained from a drop-cast CHCl$_3$/CHX (1:1 v/v) solution of [(S)-1·2]$_n$ (c = 2.5 × 10^{-4} M) on a mica surface and on a carbon-coated grid, respectively.

415 nm and a shoulder around 400 nm (Figure 6b), again showing an induced CD effect in the region where achiral OPE **2** absorbs. The variation of the induced CD effect was recorded as a function of temperature and concentration for both [(S)-1·2]$_n$ and [(R)-1·2]$_n$ assemblies. As expected, both enantiomers displayed analogous spectroscopic trends (Figure 6c). VT-CD experiments from 293 to 333 K on a solution of [1·2]$_n$ showed a gradual reduction of the CD signal at 415 nm, which is in accordance with the VT-UV−vis measurements (SI, Figure S15). Similar results were also obtained when monitoring the CD profile during dilution experiments (Figure 6d, from c = 2.5 × 10^{-4} M to c = 1.9 × 10^{-5} M). Variable-concentration CD

experiments showed a sigmoidal behavior of the intensity at 415 nm (inset of Figure 6d), which suggested that the Ur·DAP complex governs the formation of the supramolecular architectures. This was further confirmed by control steady-state UV−vis absorption experiments using solutions containing reference BOC-protected molecules **3** in the presence of linear module **2**, which displayed an absorption profile deriving from the single components. This further indicates that the formation of the Ur·DAP complex governs the formation of the supramolecular architectures. Appreciably, when the experiments were performed with [(R)-1·2]$_n$ and [(S)-1·2]$_n$ assemblies, the spectra were mirror images of each other (Figure 6).

Subsequently, the morphology of the supramolecular aggregates made of [1·2]$_n$ on mica surface (transferred from a CHCl$_3$/CHX (1:1 v/v) solution, c = 2.5 × 10^{-4} M) was studied. The TM-AFM and TEM images in Figure 6e−j showed the formation of an entangled network of fibers displaying heights ranging from 20 to 80 nm and lengths up to several μm. Although the CD spectra suggested the formation of a chiral secondary structure in a CHCl$_3$/CHX (1:1 v/v) solution, a microscopic helicity was not observed using AFM or TEM, even though it might be present at the nanoscopic level. This was also noticed for other supramolecular systems.[7b,33] The formation of fibers suggested that the higher degree of polymerization in the 1:1 v/v CHCl$_3$/CHX solution favors the development of fibers. Most likely, the solvophilic character of this solvent mixture disfavors aggregation phenomena and thus solutal instabilities.

CHX/THF: From Solution to Chiral Helices. A good compromise between solubility and nanostructuration was found in a CHX/THF (95:5 v/v) solvent mixture. Although we could not estimate the degree of association in this solvent mixture because of the presence of precipitate at the typical concentration conditions for ^{1}H NMR, a chiroptical profile similar to that obtained in CHCl$_3$/CHX (1:1 v/v) and toluene solutions was also observed for a 1:1 mixture of **1** and **2** (Figure 7d). Luminescence spectra were obtained at even more dilute concentrations (c = 3.5 × 10^{-6} M). Both compounds exhibited strong fluorescence, with related quantum yields (Φ$_{fl}$) = 0.12 and ≃ 1.0 for **1** and **2**, respectively. The absorption and emission features of OPE derivative **2** alone in the CHX/THF (95:5 v/v) mixture were red-shifted compared to those in more polar solvents such as MeOH and THF,[19b,22b] indicating a strong solvophobic-driven self-aggregation of **2**, most likely through J-type association of the aromatic rings.[34] Moreover, the emission of [(R)-1·2]$_n$ showed a weak shoulder at longer wavelengths and, compared to a solution containing only **2**, a lower quantum yield (Φ$_{fl}$ = 0.18) and a higher full width at half-maximum (fwhm), i.e., 80 nm (**2**: 62 nm, Figure 7c). The slight changes observed in the absorption and emission spectra of [(R)-1·2]$_n$ along with the lifetime values (3.4 ns for (R)-1; τ$_1$ = 1.5 ns; τ$_2$ = 3.7 ns for **2**; τ$_1$ = 1.2 ns; τ$_2$ = 4.2 ns for [(R)-1·2]$_n$) were ascribed to the presence of H-bonded self-organized structures in CHX/THF (95:5 v/v) (Figure 7a−c and SI, Figure S26c). Notably, the emission at high temperature showed a blue-shifted maximum with substantially reduced FWHM (52 nm) and the disappearance of the extended shoulder at longer wavelengths (Figure 7c). This indicated the presence of isolated units of molecule **2** in the sample, which also exhibited much higher intensity. Owing to the high quantum yield of the monomer unit **2** (Φ$_{fl}$ ≃ 1.0), its emission peak masked the signal of weakly emissive molecular species
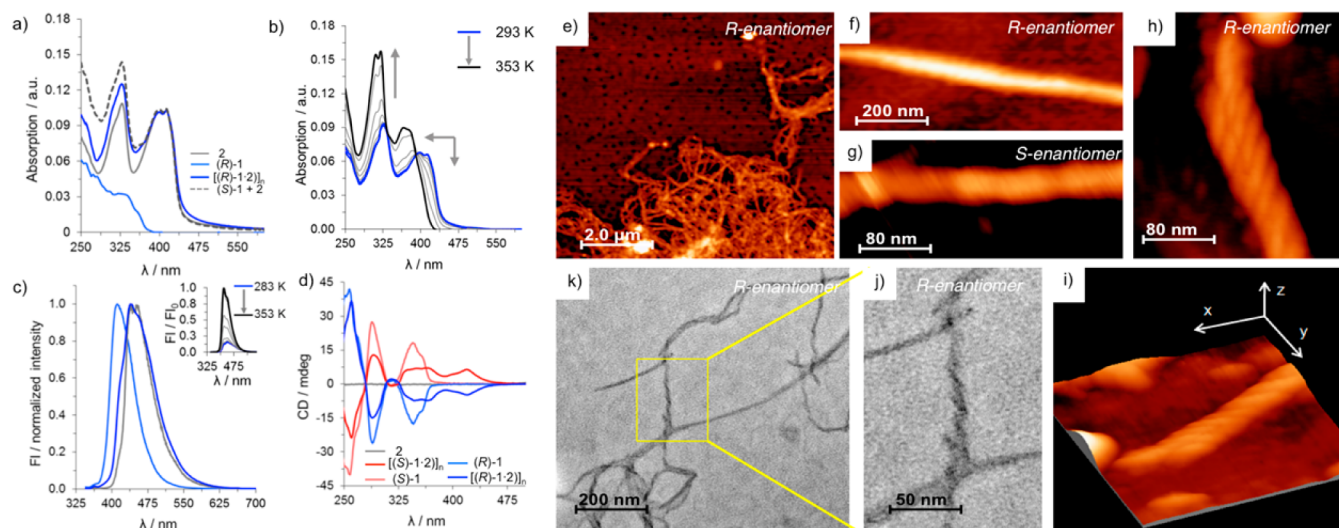
Figure 7. (a) Electronic absorption of **(R)-1** (light blue), **2** (gray), $[(R)\text{-}\mathbf{1}\cdot\mathbf{2}]_n$ (blue), and algebraic sum of **(R)-1** and **2** (dashed gray) in CHX/THF (95:5 v/v), $c = 3.5 \times 10^{-6}$ M. (b) Absorption spectral changes of 1:1 ($c = 3.5 \times 10^{-6}$ M) mixture of $[(R)\text{-}\mathbf{1}\cdot\mathbf{2}]_n$ during VT measurement. (c) Normalized fluorescence spectra of **(R)-1** (light blue), **2** (gray), and $[(R)\text{-}\mathbf{1}\cdot\mathbf{2}]_n$ (blue) and (inset) VT-emission spectral changes of $[(R)\text{-}\mathbf{1}\cdot\mathbf{2}]_n$ recorded each 10 K at a rate of 1 K/min. (d) CD spectra of **(S)-1**, **(R)-1**, **2**, $[(S)\text{-}\mathbf{1}\cdot\mathbf{2}]_n$, and $[(R)\text{-}\mathbf{1}\cdot\mathbf{2}]_n$ in CHX/THF (95:5 v/v) at 293 K ($c = 3.5 \times 10^{-6}$ M). TM-AFM (e–i), and TEM (j,k) images of nanofibers as obtained from drop-casting a CHX/THF (95:5 v/v) solution of $[(R)\text{-}\mathbf{1}\cdot\mathbf{2}]_n$ on a mica surface and on a carbon-coated grid, respectively ($c = 1.7 \times 10^{-3}$ M).

(i.e., **(R)-1**, $\Phi_{fl} = 0.12$). In order to corroborate the presence of H-bonds between molecular species **(R)-1** and **2**, a H-bond-disrupting polar solvent such as DMSO was added (5% v/v) to a solution of $[(R)\text{-}\mathbf{1}\cdot\mathbf{2}]_n$ (Figure S26a,b). Upon addition of DMSO, the absorption spectrum of $[(R)\text{-}\mathbf{1}\cdot\mathbf{2}]_n$ showed the appearance of blue-shifted bands with discernible signatures of the individual molecular units, **(R)-1** and **2** (Figure S26). The disruption of the assembly by DMSO was also observed with the VT-fluorescence experiments. Microscopic analysis of the deposited of CHX/THF (95:5 v/v) solutions containing $[(R)\text{-}\mathbf{1}\cdot\mathbf{2}]_n$ also displayed the formation of fiber-like morphologies (Figure 7e). The fibrous structures had small diameters ranging from 5 to 10 nm and average lengths between 0.8 and 3 μm. The same morphologies were also obtained upon deposition of the chiral supramolecular systems $[(S)\text{-}\mathbf{1}\cdot\mathbf{2}]_n$. Reference AFM experiments of reference racemic $[\mathbf{1}\cdot\mathbf{2}]$ polymer revealed the formation of nanofibers that macroscopically lacked an apparent chirality (SI, Figure S29). As previously mentioned, CD investigations of dilute solutions containing $[(R)\text{-}\mathbf{1}\cdot\mathbf{2}]_n$ and $[(S)\text{-}\mathbf{1}\cdot\mathbf{2}]_n$ under the same experimental conditions showed the formation of a new signal, centered at around 420 nm but presenting opposite signs (Figure 7d). This observation, together with the formation of fibrous morphologies, can be considered as a clear proof of the transfer of chirality from the molecular scale to nanostructured objects, in which the different single polymeric structures are held together by the combination of non-covalent interactions. Similar to the case of the CHCl$_3$/CHX (1:1 v/v) solution, the formation of narrow fibers from CHX/THF (95:5 v/v) suggested that, under these conditions, higher degrees of polymerization are achieved and no extensive aggregation is observed. This is probably due to the solvophilic character of these supramolecular polymers in this solvent mixture.

Nanostructuration of the Chiral Helices. Additional evidence for the formation of the fibrous aggregates in solution was obtained from SAXS, a powerful technique to determine the shape and size of colloidal, diluted, and particulate systems.[35] The SAXS pattern of a solution of $[(R)\text{-}\mathbf{1}\cdot\mathbf{2}]_n$ in CHX/THF (95:5 v/v, $c = 1.7 \times 10^{-6}$ M) is reported in Figure 8. In order to reconstruct the three-dimensional structure

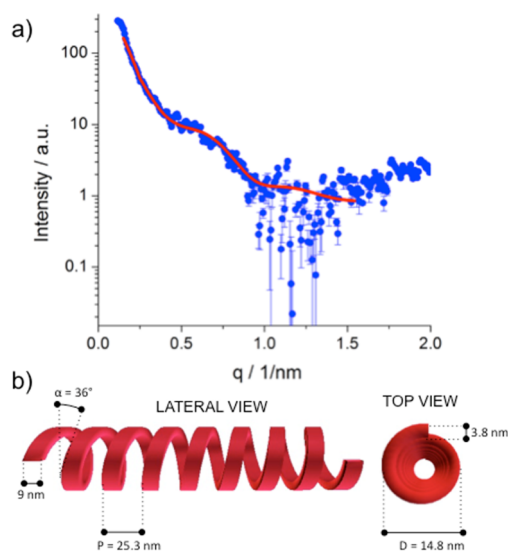**Figure 8.** (a) Experimental SAXS data (blue) obtained from a solution of $[(R)\text{-}\mathbf{1}\cdot\mathbf{2}]_n$ in CHX/THF (95:5 v/v) (298 K, $c = 1.7 \times 10^{-6}$ M) superimposed with a fitting model (red line) of a helical tape. (b) Schematic representation of the supramolecular helicoidal fibers as obtained from $[(R)\text{-}\mathbf{1}\cdot\mathbf{2}]_n$.

adopted by the supramolecular polymer, the data have been fitted by assuming homogeneous monodisperse structural models, such as cylinders, hollow cylinders, and helical bundles. The best fitting result (Figure 8a, red line) was obtained using helical superstructure models[36] resulting from the topological twisting (angle of 36°) of a 1D nanostructure featuring a ribbon-like structure (width of 8 nm). Their structural and geometrical features are depicted in Figure 8b.[37]

In order to gain insight into the molecular organization of the nanofibers, molecular modeling simulations were also carried
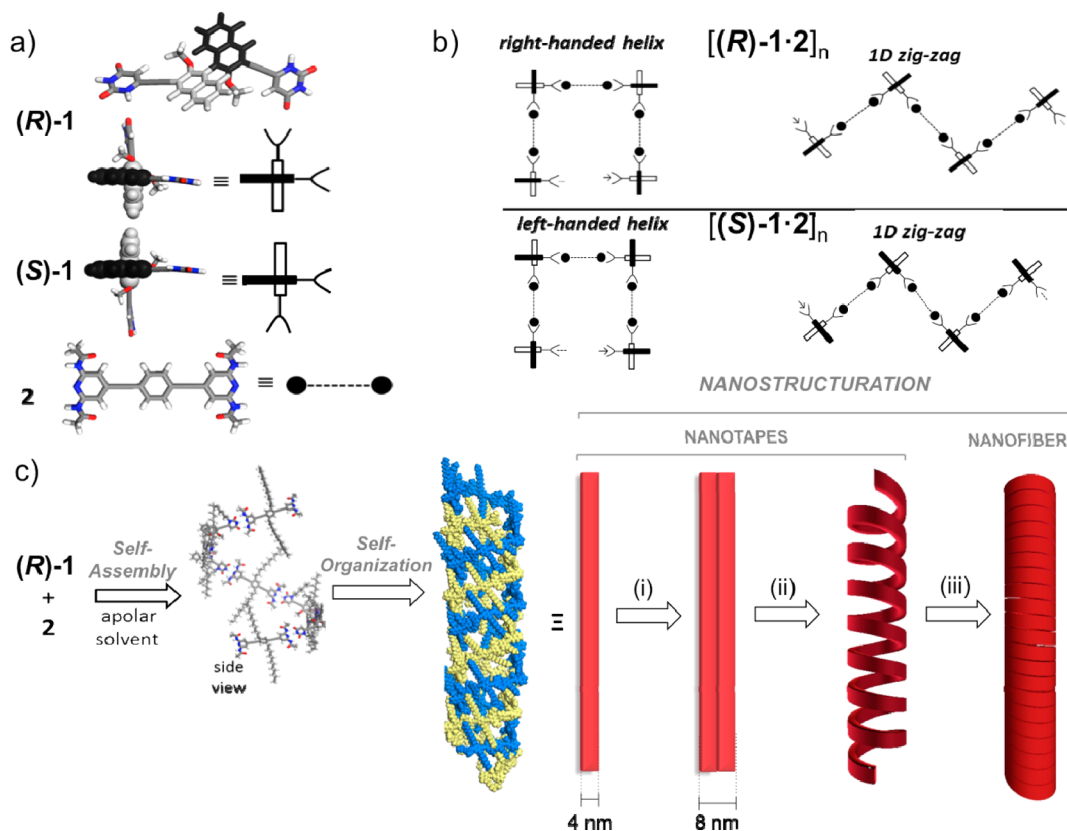
Figure 9. Molecular modeling of the supramolecular polymers of $[(R)\text{-}1\cdot2]_n$ and $[(S)\text{-}1\cdot2]_n$. (a) Side and top views of conformers of **1** along with their sketch representation (on the right). (b) Sketch of the different possible assemblies considered for the molecular mechanics (MM) simulations. (c) Proposed simulated model for self-organized nanofibers (CPK view, one helix in blue, the other in yellow, ∼15-nm-long fiber as obtained through several MM simulations cycles of the superstructure): at first, the self-assembly occurs through H-bonding between the complementary modules in a helix-type arrangement, which is right- and left-handed for $[(R)\text{-}1\cdot2]_n$ and $[(S)\text{-}1\cdot2]_n$, respectively, followed by a self-interdigitation of the single helices yielding double helix nanofibers. As observed by SAXS analysis in solution and AFM images on surfaces, it is envisaged that the individual nanofibers are organized into the final superhelical nanofibers by a possible three-step mechanism based on the formation of a tape structure (i) that will eventually twist into a single helical tape (ii) and finally dimerize into the final nanofibers structure (iii) observed by TEM and AFM.

out at the atomic level using molecular mechanics (MM). MM studies were performed using the COMPASS force field, which accurately describes the geometry and torsion potentials of phenylene ethynylene oligomers, alkyl groups, and BINOL and is appropriately optimized for modeling organic condensed-phase and H-bonded structures.[38] Figure 9 shows the structures of the studied compounds and the molecular modeling of the H-bonded bi-component supramolecular networks. Conformers of (R)-**1** and (S)-**1** possess a torsional angle between the naphthyl planes of around 96° for the *transoid* conformer (see Figure 9a for the *transoid* conformation, where the 2,2′-methoxy groups are pointing in opposite directions) and 72° for the *cisoid* conformers. For linear module **2**, the *p*-phenylene ethynylene moiety has a flat torsion potential between the phenylenes (0.5 kcal/mol barrier), which dictate through the torsional angle of the BINOL units the geometrical properties of supramolecular polymers $[(R)\text{-}1\cdot2]_n$ and $[(S)\text{-}1\cdot2]_n$. Depending on whether one naphthyl substituent of the (R)-**1** or (S)-**1** module is facing the neighboring naphthyl at each side of the linear linker (see sketch in Figure 9b where equivalent naphthyl moieties are depicted with the same black tonality), the complementary H-bonding arrangement yields two possible types of bi-component networks, namely helix or zigzag patterns (Figure 9b). Based on a series of modeled assemblies obtained by different cycles of MM simulations, we found that

square-shaped networks indeed form a helical assembly at the supramolecular level with a pitch made of tetrameric units of $[(R)\text{-}1\cdot2]_n$ (Figure 9c). In contrast, the zigzag arrangement yields the formation of one-dimensional polymer, because in this setting two equivalent naphthyl substituents face each other at each terminus of the linear unit (Figure 9b). Although this type of supramolecular organization would leave large voids in the arrangement, the presence of the C_{12} alkyl groups stabilizes the formation of supercoiled double helical cables (Figure 9c) by lateral alkyl–alkyl interdigitation. In the geometry-optimized model of $[(R)\text{-}1\cdot2]_n$ shown in Figure 9c, both molecular geometries and length of the alkyl groups govern the formation of compact double helicoidal arrangement, with a single-helix pitch of around 3.8 nm (i.e., 1.9 nm from blue helix to yellow helix in Figure 9c). The geometry of the double helix has a rectangular cross section, with a minimum distance of around 2.8 nm from side to side and a maximum distance of around 5.0 nm from corner to corner. Indeed, such compact packing is very likely more stable than the zigzag arrangement in apolar solvents, as the alkyl groups point at the outer surface of the helix. Notably, the geometrical parameters obtained from the MM simulation are strictly related to the structural data obtained from the SAXS analysis of $[(R)\text{-}1\cdot2]_n$ in a CHX/THF (95:5 v/v) solution. Indeed, the supramolecular dimerization of one of these single rectangular units through van der Waals
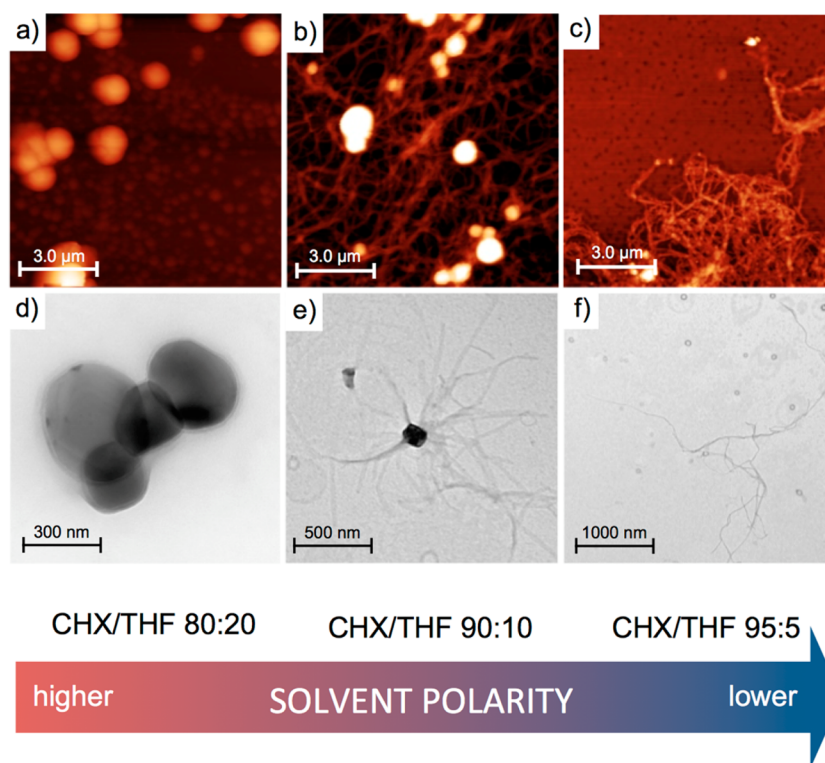
Figure 10. Nanostructuration of the supramolecular polymers into organic morphologies depending on the polarity of the drop-cast solution: TM-AFM and TEM images for (a,d) CHX/THF (80:20 v/v), (b,e) CHX/THF (90:10 v/v), and (c,f) CHX/THF (95:5 v/v).

interactions, dictated most probably by multiple interdigitation of the solubilizing alkyl chains, would lead to the formation of a flat ribbon nanostructure with dimensions comparable with those reported by the SAXS results (4 nm height and 8 nm width, Figure 9c, model (i)). The consequent twisting and dimerization (Figure 9c, steps (ii) and (iii), respectively) of the resulting ribbon would allow the formation of the supercoiled fibrous structure observed at the microscale by both TEM and AFM analysis.

From Nanospheres to Helices. To shed further light on the role of the solvent mixture giving the chiral morphologies, we investigated various solvent mixtures between CHX and THF. As in previous cases, equimolar amounts of molecular modules (*R*)-**1** or (*S*)-**1** and **2** were first dissolved into a minor volume of THF (solvent able to completely solubilize both compounds) and then diluted to the necessary volume with CHX. Aiming at favoring the formation of the most thermodynamically stable architectures, the resulting mixtures were heated and finally drop-casted onto mica surfaces for microscopic analysis, and then left to evaporate at room temperature. With more polar mixture (CHX/THF 80:20 v/v), the formation of round nanostructures was observed by TEM and TM-AFM investigations (Figure 10a,d). Through detailed TM-AFM analysis, spherical nanoparticles characterized by height from 10 to 70 nm and thickness of nm to a few tens of nm were obtained (Figure 10a). Interestingly, when a solution of $[\mathbf{1 \cdot 2}]_n$ was transferred from a CHX/THF (90:10 v/v) solution to the mica surface, globular aggregates were predominantly observed, but fibrous material also started to appear (Figure 10b,e). Specifically, the deposited material is characterized by the presence of spherical morphologies that peripherally expose fibrous ramifications, with diameters between 5 and 50 nm and length up to several *μ*m. With

respect to the fibrous morphologies obtained from the CHX/THF (95:5 v/v) solutions, the ramifications displayed some substantial structural differences, as they appear as bamboo-like structures. In both cases, SAXS measurements did not reveal any periodicity or formation of homogeneous structures. Whereas in the more polar solvent mixture (CHX/THF 80:20 v/v) the aggregation seems to be essentially governed by the concentration-driven solutal instability, increasing the apolar character of the solvent enhances the degree of polymerization, favoring the formation of long supramolecular polymers as the solvent evaporates, and thus the formation of long fibers.

■ CONCLUSIONS

We have presented the synthesis and characterization of novel molecular modules carrying heterocomplementary H-bonding recognition motifs. The building block is composed of a BINOL unit which, through its atropoisomers (*R*) and (*S*), served as a chiral unit. Together with a complementary H-bond partner, an achiral linear OPE chromophore, the modules underwent self-assembly through triple H-bonding interactions. The association strength of the triply bonded structures was determined in $CDCl_3$, $CDCl_3/CHX\text{-}d_{12}$, and $Tol\text{-}d_8$, together with the binding stoichiometry. Through a simple experimental model, we have shown that, together with the association strength, the vapor tension of a given solvent governs the degree of polymerization under evaporation conditions and thus the nanostructuration of an organic morphology. In particular, solvents favoring strong H-bonded complexes and displaying high vapor pressures induce the formation of high degrees of polymerization. Owing to the chromophore unit, it was possible to follow the self-assembly through UV−vis, CD, and fluorescence spectroscopy. Notably, through concentra-

tion-dependent CD spectroscopy, an isodesmic polymerization mechanism was uncovered. The self-assembled supramolecular polymer has been transferred onto the surface for microscopic investigations through AFM and TEM measurements. Nanostructuration afforded nanorods (from CHCl$_3$), nanofibers (CHCl$_3$/CHX), nanospheres (CHX/THF 80:20 v/v), hybrid nanosphere/nanofibers (CHX/THF 90:10 v/v), and finally helical nanofibers (CHX/THF 95:5 v/v). The self-organization and the chiral transfer from solution to surface were also studied with the aid of SAXS analysis and molecular modeling in order to gain insight into the nanostructuration mechanisms of the material into superhelical nanofibers. These results suggest that solvents exhibiting high vapor tension and favoring high degrees of polymerization mold the formation of fibrous morphologies apparently expressing chiral morphologies at the microscale. On the other hand, solvents favoring low degree of polymerization with low vapor tensions yield amorphous morphologies (Tol). The solvophilic character of a given solvent mixture disfavors aggregation phenomena, thus reducing solutal instability and driving the formation of supramolecularly controlled nanostructures. Taken in concert, our experiments showed that the choice of solvent is crucial to dictate the polymorphism of the nanomaterial and the transmission of molecular chirality at higher scales. In particular, an optimal balance among high degree of association, solvent vapor pressure, and the solvophobic/solvophilic properties needs to be accomplished in order to control the formation of organic morphologies.

ASSOCIATED CONTENT

Ⓢ Supporting Information

Synthetic protocols, spectroscopic characterizations, and titration experiments. The Supporting Information is available free of charge on the ACS Publications website at DOI: 10.1021/jacs.5b02448.

AUTHOR INFORMATION

Corresponding Authors

*mathieu.surin@umons.ac.be
*davide.bonifazi@unamur.be

Author Contributions

‡L.Đ. and T.M. contributed equally.

Notes

The authors declare no competing financial interest.

ACKNOWLEDGMENTS

REFERENCES

(1) (a) Lehn, J. M. *Science* **2002**, *295*, 2400−2403. (b) Lehn, J. M. *Proc. Natl. Acad. Sci. U.S.A.* **2002**, *99*, 4763−4768. (c) Whitesides, G. M.; Grzybowski, B. *Science* **2002**, *295*, 2418−2421.

(2) (a) Aida, T.; Meijer, E. W.; Stupp, S. I. *Science* **2012**, *335*, 813−817. (b) Busseron, E.; Ruff, Y.; Moulin, E.; Giuseppone, N. *Nanoscale* **2013**, *5*, 7098−7140. (c) Santhosh Babu, S.; Praveen, V. K.; Ajayaghosh, A. *Chem. Rev.* **2014**, *114*, 1973−2129. (d) Stupp, S. I.; Palmer, L. C. *Chem. Mater.* **2014**, *26*, 507−518. (e) Dong, R.; Zhou, Y.; Huang, X.; Zhu, X.; Lu, Y.; Shen, J. *Adv. Mater.* **2015**, *27*, 498−526.

(3) (a) Santhosh Babu, S.; Prasanthkumar, S.; Ajayaghosh, A. *Angew. Chem., Int. Ed.* **2012**, *51*, 1766−1776. (b) Ceroni, P.; Credi, A.; Venturi, M. *Chem. Soc. Rev.* **2014**, *43*, 4068. (c) Praveen, V. K.; Ranjith, C.; Bandini, E.; Ajayaghosh, A.; Armaroli, N. *Chem. Soc. Rev.* **2014**, *43*, 4222−4242. (d) Xu, J.; Semin, S.; Rasing, T.; Rowan, A. E. *Small* **2014**, *11*, 1113−1129. (e) Yan, Q.; Luo, Z.; Cai, K.; Ma, Y.; Zhao, D. *Chem. Soc. Rev.* **2014**, *43*, 4199−4221.

(4) (a) Bunz, U. H. F. *Chem. Rev.* **2000**, *100*, 1605−1644. (b) Ajayaghosh, A.; Varghese, R.; Praveen, V. K.; Mahesh, S. *Angew. Chem., Int. Ed.* **2006**, *45*, 3261−3264. (c) Garcia, F.; Sanchez, L. *J. Am. Chem. Soc.* **2012**, *134*, 734−742. (d) Ajayaghosh, A.; Varghese, R.; Mahesh, S.; Praveen, V. K. *Angew. Chem., Int. Ed.* **2006**, *45*, 7729−7732.

(5) (a) Ajayaghosh, A.; Praveen, V. K. *Acc. Chem. Res.* **2007**, *40*, 644−656. (b) Schenning, A. P.; Meijer, E. W. *Chem. Commun.* **2005**, 3245−3258. (c) Moulin, E.; Cid, J. J.; Giuseppone, N. *Adv. Mater.* **2013**, *25*, 477−487.

(6) (a) Hill, J. P.; Jin, W.; Kosaka, A.; Fukushima, T.; Ichihara, H.; Shimomura, T.; Ito, K.; Hashizume, T.; Ishii, N.; Aida, T. *Science* **2004**, *304*, 1481−1483. (b) Wu, J.; Pisula, W.; Müllen, K. *Chem. Rev.* **2007**, *107*, 718−747. (c) Ito, S.; Herwig, P. T.; Böhme, T.; Rabe, J. P.; Rettig, W.; Müllen, K. *J. Am. Chem. Soc.* **2000**, *122*, 7698−7706. (d) Dossel, L. F.; Kamm, V.; Howard, I. A.; Laquai, F.; Pisula, W.; Feng, X.; Li, C.; Takase, M.; Kudernac, T.; De Feyter, S.; Müllen, K. *J. Am. Chem. Soc.* **2012**, *134*, 5876−5886. (e) Seyler, H.; Purushothaman, B.; Jones, D. J.; Holmes, A. B.; Wong, W. W. H. *Pure Appl. Chem.* **2012**, *84*, 1047−1067.

(7) (a) Elacqua, E.; Lye, D. S.; Weck, M. *Acc. Chem. Res.* **2014**, *47*, 2405−16. (b) Jonkheijm, P.; Hoeben, F. J. M.; Kleppinger, R.; van Herrikhuyzen, J.; Schenning, A. P. H. J.; Meijer, E. W. *J. Am. Chem. Soc.* **2003**, *125*, 15941−15949. (c) Puigmartí-Luis, J.; Minoia, A.; Pérez del Pino, Á.; Ujaque, G.; Rovira, C.; Lledos, A.; Lazzaroni, R.; Amabilino, D. B. *Chem.—Eur. J.* **2006**, *12*, 9161−9175. (d) Chithra, P.; Varghese, R.; Divya, K. P.; Ajayaghosh, A. *Chem.—Asian J.* **2008**, *3*, 1365−1373. (e) Puigmartí-Luis, J.; Pérez del Pino, Á.; Laukhina, E.; Esquena, J.; Laukhin, V.; Rovira, C.; Vidal-Gancedo, J.; Kanaras, A. G.; Nichols, R. J.; Brust, M.; Amabilino, D. B. *Angew. Chem., Int. Ed.* **2008**, *47*, 1861−1865. (f) Yagai, S.; Aonuma, H.; Kikkawa, Y.; Kubota, S.; Karatsu, T.; Kitamura, A.; Mahesh, S.; Ajayaghosh, A. *Chem.—Eur. J.* **2010**, *16*, 8652−8661. (g) Gopal, A.; Varghese, R.; Ajayaghosh, A. *Chem.—Asian J.* **2012**, *7*, 2061−2067.

(8) (a) Pirondini, L.; Stendardo, A. G.; Geremia, S.; Campagnolo, M.; Samorì, P.; Rabe, J. P.; Fokkens, R.; Dalcanale, E. *Angew. Chem., Int. Ed.* **2003**, *42*, 1384−1387. (b) Surin, M.; Samorì, P.; Jouaiti, A.; Kyritsakas, N.; Hosseini, M. W. *Angew. Chem., Int. Ed.* **2007**, *46*, 245−249. (c) Northrop, B. H.; Yang, H. B.; Stang, P. J. *Chem. Commun.* **2008**, *45*, 5896−5908. (d) Imaz, I.; Rubio-Martinez, M.; Saletra, W. J.; Amabilino, D. B.; Maspoch, D. *J. Am. Chem. Soc.* **2009**, *131*, 18222−18223. (e) Northrop, B. H.; Zheng, Y. R.; Chi, K. W.; Stang, P. J. *Acc. Chem. Res.* **2009**, *42*, 1554−1563. (f) Ciesielski, A.; Piot, L.; Samorì, P.; Jouaiti, A.; Hosseini, M. W. *Adv. Mater.* **2009**, *21*, 1131−1136. (g) El Garah, M.; Ciesielski, A.; Marets, N.; Bulach, V.; Hosseini, M. W.; Samorì, P. *Chem. Commun.* **2014**, *50*, 12250−12253. (h) Caricato, M.; Delforge, A.; Bonifazi, D.; Dondi, D.; Mazzanti, A.; Pasini, D. *Org. Biomol. Chem.* **2015**, *13*, 3593−601.

(9) Lehn, J.-M. *Angew. Chem., Int. Ed.* **1988**, *27*, 89−112.

(10) (a) Brunsveld, L.; Vekemans, J. A. J. M.; Hirschberg, J. H. K. K.; Sijbesma, R. P.; Meijer, E. W. *Proc. Natl. Acad. Sci. U.S.A.* **2002**, *99*, 4977−4982. (b) Amabilino, D. B.; Stoddart, J. F.; Williams, D. J. *Chem.*

Mater. **1994**, *6*, 1159–1167. (c) Bowden, N. *Science* **1997**, *276*, 233–235. (d) Orr, G. W. *Science* **1999**, *285*, 1049–1052. (e) Pérez-García, L.; Amabilino, D. B. *Chem. Soc. Rev.* **2002**, *31*, 342–356. (f) Pérez-García, L.; Amabilino, D. B. *Chem. Soc. Rev.* **2007**, *36*, 941–967. (g) Gomar-Nadal, E.; Puigmartí-Luis, J.; Amabilino, D. B. *Chem. Soc. Rev.* **2008**, *37*, 490–504. (h) Yagai, S.; Yamauchi, M.; Kobayashi, A.; Karatsu, T.; Kitamura, A.; Ohba, T.; Kikkawa, Y. *J. Am. Chem. Soc.* **2012**, *134*, 18205–18208. (i) Pfukwa, R.; Kouwer, P. H. J.; Rowan, A. E.; Klumperman, B. *Angew. Chem., Int. Ed.* **2013**, *52*, 11040–11044.

(11) (a) Li, M.; Xu, S.; Kumacheva, E. *Macromolecules* **2000**, *33*, 4972–4978. (b) Carvalho, A. J.; Pereira-da-Silva, M. A.; Faria, R. M. *Eur. Phys. J. E* **2006**, *20*, 309–315. (c) Thiele, U.; Vancea, I.; Archer, A. J.; Robbins, M. J.; Frastia, L.; Stannard, A.; Pauliac-Vaujour, E.; Martin, C. P.; Blunt, M. O.; Moriarty, P. J. *J. Phys.: Condens. Matter* **2009**, *21*, No. 264016. (d) Li, B.; Puigmartí-Luis, J.; Jonas, A. M.; Amabilino, D. B.; De Feyter, S. *Chem. Commun.* **2014**, *50*, 13216–13219.

(12) (a) Voorhees, P. W. *J. Stat. Phys.* **1985**, *38*, 231–252. (b) Mahesh, S.; Gopal, A.; Thirumalai, R.; Ajayaghosh, A. *J. Am. Chem. Soc.* **2012**, *134*, 7227–7230.

(13) (a) Reiter, G. *Phys. Rev. Lett.* **1992**, *68*, 75–78. (b) Maeda, H. *Langmuir* **2000**, *16*, 9977–9982. (c) Gonuguntla, M.; Sharma, A. *Langmuir* **2004**, *20*, 3456–3463.

(14) (a) Karthaus, O.; Gråsjö, L.; Maruyama, N.; Shimomura, M. *Thin Solid Films* **1998**, *327–329*, 829–832. (b) Weh, L. *J. Colloid Interface Sci.* **2001**, *235*, 210–217.

(15) (a) van Dijk, M. A.; van den Berg, R. *Macromolecules* **1995**, *28*, 6773–6778. (b) Kim, G.; Libera, M. *Macromolecules* **1998**, *31*, 2569–2577.

(16) Marangoni, T.; Mezzasalma, S. A.; Llanes-Pallas, A.; Yoosaf, K.; Armaroli, N.; Bonifazi, D. *Langmuir* **2011**, *27*, 1513–1523.

(17) (a) Terfort, A.; Bowden, N.; Whitesides, G. M. *Nature* **1997**, *386*, 162–164. (b) Puigmartí-Luis, J.; Pérez del Pino, Á.; Laukhin, V.; Feldborg, L. N.; Rovira, C.; Laukhina, E.; Amabilino, D. B. *J. Mater. Chem.* **2010**, *20*, 466. (c) Gillissen, M. A. J.; Koenigs, M. M. E.; Spiering, J. J. H.; Vekemans, J. A. J. M.; Palmans, A. R. A.; Voets, I. K.; Meijer, E. W. *J. Am. Chem. Soc.* **2014**, *136*, 336–343. (d) Hollamby, M. J.; Karny, M.; Bomans, P. H. H.; Sommerdijk, N. A. J. M.; Saeki, A.; Seki, S.; Minamikawa, H.; Grillo, I.; Pauw, B. R.; Brown, P.; Eastoe, J.; Möhwald, H.; Nakanishi, T. *Nat. Chem.* **2014**, *6*, 690–696.

(18) (a) Amabilino, D. B.; Veciana, J. *Top. Curr. Chem.* **2006**, *265*, 253–302. (b) Palmans, A. R. A.; Meijer, E. W. *Angew. Chem., Int. Ed.* **2007**, *46*, 8948–8968. (c) Crassous, J. *Chem. Soc. Rev.* **2009**, *38*, 830–845. (d) Amabilino, D. B. *Chem. Soc. Rev.* **2009**, *38*, 669–670. (e) Coquerel, G.; Amabilino, D. B. The Nanoscale Aspects of Chirality in Crystal Growth: Structure and Heterogeneous Equilibria. In *Chirality at the Nanoscale: Nanoparticles, Surfaces, Materials and More*; Amabilino, D. B., Ed.; Wiley: Weinheim, 2009; pp 305–348. (f) Zhang, L.; Qin, L.; Wang, X.; Cao, H.; Liu, M. *Adv. Mater.* **2014**, *26*, 6959–6964.

(19) (a) Mohnani, S.; Llanes-Pallas, A.; Bonifazi, D. *Pure Appl. Chem.* **2010**, *82*, 917–929. (b) Yoosaf, K.; Llanes-Pallas, A.; Marangoni, T.; Belbakra, A.; Marega, R.; Botek, E.; Champagne, B.; Bonifazi, D.; Armaroli, N. *Chem.—Eur. J.* **2011**, *17*, 3262–3273. (c) Llanes-Pallas, A.; Yoosaf, K.; Traboulsi, H.; Mohanraj, J.; Seldrum, T.; Dumont, J.; Minoia, A.; Lazzaroni, R.; Armaroli, N.; Bonifazi, D. *J. Am. Chem. Soc.* **2011**, *133*, 15412–15424. (d) Maggini, L.; Marangoni, T.; Georges, B.; Malicka, J. M.; Yoosaf, K.; Minoia, A.; Lazzaroni, R.; Armaroli, N.; Bonifazi, D. *Nanoscale* **2013**, *5*, 634–645.

(20) (a) Bonifazi, D.; Mohnani, S.; Llanes-Pallas, A. *Chem.—Eur. J.* **2009**, *15*, 7004–7025. (b) Marangoni, T.; Bonifazi, D. *Nanoscale* **2013**, *5*, 8837–8851.

(21) Yoosaf, K.; Belbakra, A.; Armaroli, N.; Llanes-Pallas, A.; Bonifazi, D. *Chem. Commun.* **2009**, 2830–2832.

(22) (a) Piot, L.; Palma, C.-A.; Llanes-Pallas, A.; Prato, M.; Szekrényes, Z.; Kamarás, K.; Bonifazi, D.; Samorì, P. *Adv. Funct. Mater.* **2009**, *19*, 1207–1214. (b) Llanes-Pallas, A.; Palma, C. A.; Piot, L.; Belbakra, A.; Listorti, A.; Prato, M.; Samorì, P.; Armaroli, N.; Bonifazi, D. *J. Am. Chem. Soc.* **2009**, *131*, 509–520. (c) Szekrényes, Z.; Kamarás, K.; Tarczay, G.; Llanes-Pallas, A.; Marangoni, T.; Bonifazi,

D.; Björk, J.; Hanke, F.; Persson, M. *J. Phys. Chem. C* **2012**, *116*, 4626–4633.

(23) Llanes-Pallas, A.; Matena, M.; Jung, T.; Prato, M.; Stohr, M.; Bonifazi, D. *Angew. Chem., Int. Ed.* **2008**, *47*, 7726–7730.

(24) (a) Brunel, J. M. *Chem. Rev.* **2005**, *105*, 857–898. (b) Caricato, M.; Sharma, A. K.; Coluccini, C.; Pasini, D. *Nanoscale* **2014**, *6*, 7165–7174. (c) Hill, D. J.; Moore, J. S. *Proc. Natl. Acad. Sci. U.S.A.* **2002**, *99*, 5053–5057.

(25) Hua, J.; Lin, W. *Org. Lett.* **2004**, *6*, 861–864.

(26) Cook, J. L.; Hunter, C. A.; Low, C. M.; Perez-Velasco, A.; Vinter, J. G. *Angew. Chem., Int. Ed.* **2007**, *46*, 3706–3709.

(27) Beijer, F. H.; Sijbesma, R. P.; Vekemans, J. A. J. M.; Meijer, E. W.; Kooijman, H.; Spek, A. L. *J. Org. Chem.* **1996**, *61*, 6371–6380.

(28) (a) Ciferri, A. *Macromol. Rapid Commun.* **2002**, *23*, 511–529. (b) Michelsen, U.; Hunter, C. A. *Angew. Chem., Int. Ed.* **2000**, *39*, 764–767.

(29) (a) Macchioni, A.; Ciancaleoni, G.; Zuccaccia, C.; Zuccaccia, D. *Chem. Soc. Rev.* **2008**, *37*, 479–489. (b) Avram, L.; Cohen, Y. *Chem. Soc. Rev.* **2014**, *44*, 586–602. (c) Cohen, Y.; Avram, L.; Frish, L. *Angew. Chem., Int. Ed.* **2005**, *44*, 520–554.

(30) (a) Li, B.; Puigmartí-Luis, J.; Jonas, A. M.; Amabilino, D. B.; De Feyter, S. *Chem. Commun.* **2014**, *50*, 13216–13219. (b) Grosso, D.; Cagnol, F.; Soler-Illia, G. J. d. A. A.; Crepaldi, E. L.; Amenitsch, H.; Brunet-Bruneau, A.; Bourgeois, A.; Sanchez, C. *Adv. Funct. Mater.* **2004**, *14*, 309–322. (c) Brinker, C. J.; Lu, Y.; Sellinger, A.; Fan, H. *Adv. Mater.* **1999**, *11*, 579–585.

(31) (a) Sijbesma, R. P. *Science* **1997**, *278*, 1601–1604. (b) Brunsveld, L.; Folmer, B. J. B.; Meijer, E. W.; Sijbesma, R. P. *Chem. Rev.* **2001**, *101*, 4071–4098. (c) De Greef, T. F.; Smulders, M. M.; Wolffs, M.; Schenning, A. P.; Sijbesma, R. P.; Meijer, E. W. *Chem. Rev.* **2009**, *109*, 5687–5754.

(32) While the solubility of compound **2** in toluene is low, it increases once 1 equiv of compound **1** is added.

(33) Surin, M.; Janssen, P. G. A.; Lazzaroni, R.; Leclère, P.; Meijer, E. W.; Schenning, A. P. H. *J. Adv. Mater.* **2009**, *21*, 1126–1130.

(34) (a) Spano, F. C. *Acc. Chem. Res.* **2010**, *43*, 429–439. (b) Zhao, Y. S.; Fu, H.; Peng, A.; Ma, Y.; Xiao, D.; Yao, J. *Adv. Mater.* **2008**, *20*, 2859–2876.

(35) (a) Roe, R. J. *Methods of X-ray and neutron scattering in polymer science.* Oxford University Press: New York, 2000. (b) Patterson, J. P.; Robin, M. P.; Chassenieux, C.; Colombani, O.; O'Reilly, R. K. *Chem. Soc. Rev.* **2014**, *43*, 2412. (c) Otto Glatter, O. K. *Small Angle X-ray Scattering.* Academic Press: London, 1982.

(36) Teixeira, C. V.; Amenitsch, H.; Fukushima, T.; Hill, J. P.; Jin, W.; Aida, T.; Hotokka, M.; Linden, M. *J. Appl. Crystallogr.* **2010**, *43*, 850–857.

(37) In order to elucidate the geometric organization of the self-assembled molecular models along the twisted ribbon system, more complex fitting models taking into account also its possible internal structure were also used. However, the results were not statistically significant, and thus they were not considered.

(38) (a) Sun, H. *J. Phys. Chem. B* **1998**, *102*, 7338–7364. (b) Ren, Z.; Zeng, X.; Yang, X.; Ma, D.; Hsu, S. L. *Polymer* **2005**, *46*, 12337–12347. (c) Ziegler, A.; Mamdouh, W.; Ver Heyen, A.; Surin, M.; Uji-i, H.; Abdel-Mottaleb, M. M. S.; De Schryver, F. C.; De Feyter, S.; Lazzaroni, R.; Höger, S. *Chem. Mater.* **2005**, *17*, 5670–5683. (d) Lei, S.; Ver Heyen, A.; De Feyter, S.; Surin, M.; Lazzaroni, R.; Rosenfeldt, S.; Ballauff, M.; Lindner, P.; Mossinger, D.; Höger, S. *Chem.—Eur. J.* **2009**, *15*, 2518–2535.